RESEARCH ARTICLE | NOVEMBER 04 2024

Mode decomposition to identify oscillation patterns of flexible aeroshell

Special Collection: Fluid-Structure Interaction

Sanjoy Kumar Saha (サハサンジョイクマー) ; Yusuke Takahashi (高橋裕介)

Physics of Fluids 36, 116108 (2024)
https://doi.org/10.1063/5.0235384

Physics of Fluids ARTICLE pubs.aip.org/aip/pof

Mode decomposition to identify oscillation patterns of flexible aeroshell

Cite as: Phys. Fluids 36, 116108 (2024); doi: 10.1063/5.0235384
Submitted: 27 August 2024 · Accepted: 16 October 2024 ·
Published Online: 4 November 2024

View Online Export Citation CrossMark

Sanjoy Kumar Saha (サハサンジョイクマー)[1,a] and Yusuke Takahashi (高橋裕介)[2,b]

AFFILIATIONS

[1]Graduate School of Engineering, Hokkaido University, Kita 13 Nishi 8, Kita-ku, Sapporo 060-8628, Hokkaido, Japan
[2]Faculty of Engineering, Hokkaido University, Kita 13 Nishi 8, Kita-ku, Sapporo 060-8628, Hokkaido, Japan

Note: This paper is part of the special topic, Fluids-Structure Interaction.
[a)]**Author to whom correspondence should be addressed:** sanjoysaha.cuet@gmail.com
[b)]**Electronic mail:** ytakahashi@eng.hokudai.ac.jp

ABSTRACT

Flexible aeroshells, featuring deformable membrane surfaces supported by pressurized gas, offer a novel re-entry system for high-altitude deceleration during re-entry. The flexibility of structural components introduces unique challenges in predicting aerodynamic behavior, as deformations can significantly alter the flow field, affecting pressure distribution and potentially causing aerodynamic instabilities. Therefore, coupled analysis is crucial to ensure the performance reliability of inflatable aeroshells. This study investigates the unsteady aerodynamic behavior, considering structural deformation in a two-way partitioned coupled manner in transonic flow. The dominant deformation patterns are identified using dynamic mode decomposition and the greedy compressive sensing algorithm. The findings reveal that the primary deformation pattern combines axial deformation and swing oscillation. The dominant oscillation frequencies remain different from the eigenfrequencies, indicating that the aerodynamic force is the primary driving force of such oscillations. The time evolution of these dominant modes indicates purely oscillatory behavior rather than increasing or decreasing trends. These insights are critical for the design and reliability assessment of inflatable aeroshells in varying aerodynamic environments.

I. INTRODUCTION

Inflatable or flexible aeroshells represent a novel approach to spacecraft design, offering a unique combination of flexibility, lightweight construction, and aerodynamic performance. The flexibility of such an aeroshell enhances payload capacity, improves aerodynamic performance, and reduces costs. Additionally, their adaptability to various mission types and increased safety make them vital for robotic and human space exploration endeavors. These innovations open new possibilities for mission architectures, enhancing our ability to explore and utilize space. Inflatable aeroshell technology has been extensively researched through wind tunnel experiments and atmospheric flight tests for various aerodynamic shapes with notable projects including hypersonic and supersonic inflatable aerodynamic decelerators, inflatable re-entry and descent technology, and Membrane Aeroshell for Atmospheric-entry Capsule (MAAC).[1–8] The MAAC project focuses on developing a thin membrane inflatable aeroshell combining a flexible membrane supported by a single inflatable torus to maintain its shape, as illustrated in Fig. 1. Numerous flight experiments have employed scientific balloons and rockets to assess the viability of utilizing a membrane aeroshell for deceleration. In 2012, a flight test revealed that the attitude of the aeroshell becomes unstable when operating at low Mach numbers, and substantial aerodynamic forces and fluctuations in inflation pressure can lead to the collapse of the aeroshell.[9] The deformation of the membrane surface under the peak freestream dynamic pressure resulted in a change in the flare angle, preventing the structure from regaining its original shape thereafter.[10] Such irreversible deformation has significant implications for the overall aerodynamic performance of the aeroshell and also can drastically influence the attitude stability and aerodynamic characteristics during re-entry.

Furthermore, discrepancies were observed in the drag coefficient profiles between flight tests and wind tunnel experiments, likely due to the flexible nature of the membrane.[11,12] This flexibility is highly sensitive to flow conditions that differ between controlled environments and real flight scenarios and makes the membrane structure susceptible to deformation, leading to potential instabilities and increased thermal loads due to turbulence effects.[13,14] At transonic speeds, aerodynamic stresses on the aeroshell are very intense, resulting in

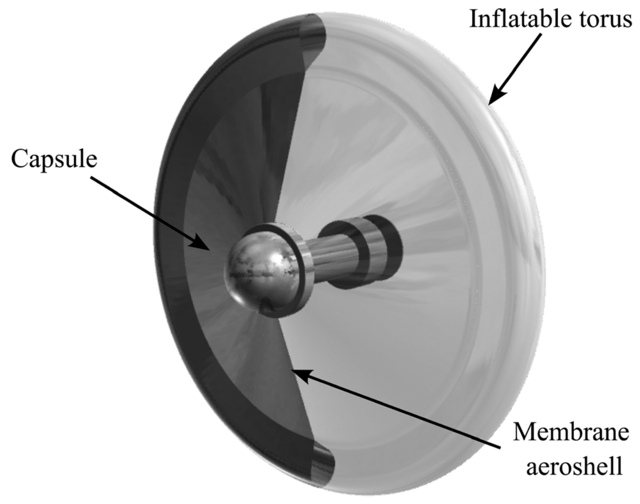

FIG. 1. Inflatable membrane aeroshell.

frequent structural failures owing to aeroelastic interactions.[15] Despite the observations of these failures, a thorough understanding of the underlying mechanisms remains inadequate. To address these challenges and improve predictive models, coupled studies must be conducted that account for the feedback impact of structural deformation.

Studying the oscillation behavior in transonic flow is essential for ensuring structural integrity and stability, as such oscillations can lead to dynamic instabilities such as flutter and divergence, which may cause structural failure.[16] In flutter instability, aerodynamic forces and structural oscillations couple, causing energy exchange that can grow into large amplitude oscillations and eventually cause structural failure. Along with strong aerodynamic forces, shock wave interactions and boundary layer separation may lead to significant unsteady oscillations. If the excitation frequencies of such oscillations match the natural frequencies of the capsule motion, resonance phenomena occur that further amplify these oscillations.[17] To address the oscillatory behavior and its impact on aeroshell performance, it is crucial to understand how these oscillations are induced by the complex interactions between aerodynamic forces and structural dynamics in the transonic regime. Moreover, it aids in understanding load variations, designing effective active control systems to dampen undesirable oscillations, and reliable deployment and operation of the aeroshell.

Ground experiments are insufficient for comprehensive multiphysics analysis of aeroshells due to challenges in accurately replicating atmospheric and flow conditions, thermal environments, and dynamic responses.[18] Scaling and boundary effects in experimental setups can alter the results, and the complex interactions between fluid dynamics, structural responses, and thermal loads are difficult to fully capture. Numerical simulations complement ground tests by providing high-fidelity data and enabling the study of a broader range of scenarios, ensuring more accurate and comprehensive analysis. However, numerical simulations that consider multiple physical domains usually produce large volumes of data, and handling such large datasets can be challenging. Coupled analyses, by definition, entail unsteady behavior, such as flutter or limit-cycle oscillations, which make understanding difficult. To simplify complex flows into manageable, low-dimensional representations that capture the dominant dynamic structures, techniques such as proper orthogonal decomposition (POD) and dynamic mode decomposition (DMD) are commonly used in the fluid dynamics community. POD prioritizes modes based on their energy content, which may not always be the most suitable criterion, as energy levels do not necessarily highlight the most relevant flow structures. On the other hand, DMD identifies modes based on their characteristic frequencies, decomposing large-scale spatiotemporal data into distinct spatial and temporal modes, making it more suitable for this study.

DMD has been applied to various flow configurations, including cavity flows, shock wave boundary layer interactions, and jet flows. Different DMD variants, such as optimal mode decomposition and noise-robust methods, have been developed to enhance their accuracy and applicability in dealing with measurement errors and other challenges. This study opted for the exact version of the DMD formulation proposed by Tu[19] considering the large dimension of this problem. Therefore, in this context, the main objective of the present work is to apply the DMD algorithm to the numerical deformation data extracted from fluid–structure interaction (FSI) simulations of an inflatable aeroshell to unveil its spatial patterns and temporal behavior to elucidate the oscillation behavior under the transonic flow regime.

II. MATHEMATICAL MODELS

A. Fluid domain

The dynamics of a viscous, compressible, Newtonian fluid are described by the Navier–Stokes equations, which are typically formulated using an Eulerian framework. In fluid–structure interaction problems, considering mesh motion is necessary since it involves moving boundaries at the common interface between the domains. Consequently, the Navier–Stokes equations are reformulated within an arbitrary Lagrangian–Eulerian (ALE) description of the motion.[20] By defining a conservative variable $\mathbf{U} = (\rho, \rho \mathrm{v}, \rho E)$, we can express the Navier–Stokes equations based on ALE system as[21,22]

$$\frac{\partial \mathbf{U}}{\partial t} + \nabla \cdot \mathbf{F}^{\mathbf{C}}_{\mathrm{ALE}}(\mathbf{U}) = \nabla \cdot \mathbf{F}^{\mathrm{v}}(\mathbf{U}), \quad \text{in a domain } t > 0, \tag{1}$$

where the vector $\mathbf{U}$ indicates the solution vector of unknowns to be determined. The vector $\mathbf{F}^{\mathrm{c}}$ represents advective fluxes, whereas $\mathbf{F}^{\mathrm{v}}$ refers to viscous fluxes, and is described as in the following equations:

$$\mathbf{F}^{\mathbf{C}}_{\mathrm{ALE}}(\mathbf{U}) = \begin{pmatrix} \rho(\mathbf{v} - \dot{u}_{\mathrm{mesh}}) \\ \rho \otimes (\mathbf{v} - \dot{u}_{\mathrm{mesh}}) + \boldsymbol{I}p \\ \rho(\mathbf{v} - \dot{u}_{\mathrm{mesh}})E + p\mathbf{v} \end{pmatrix}, \tag{2}$$

$$\mathbf{F}^{\mathrm{v}}(\mathbf{U}) = \begin{pmatrix} 0 \\ \boldsymbol{\tau} \\ \boldsymbol{\tau} \cdot \mathbf{v} + \mu C_p \nabla T \end{pmatrix}. \tag{3}$$

In this context, u_{mesh} denotes the displacements of the mesh nodes, $\dot{u}_{\mathrm{mesh}}$ is the mesh velocity, p represents the static pressure, and I denotes the identity matrix. μ stands for the dynamic viscosity of the fluid, and C_p indicates the specific heat at constant pressure, while T signifies the temperature. In addition, $\mathbf{v} = (v_1, v_2, v_3)$ is the vector of flow velocities, E represents the total energy of the flow per unit mass, and τ denotes the viscous stress tensor.

B. Structural domain

The structural response of a flexible three-dimensional solid is described by the equation of motion, which can be expressed in spatially discretized form as follows:

$$[M]\{\ddot{u}\} + [C]\{\dot{u}\} + [K]\{u\} = \{F\}, \tag{4}$$

where $[M]$ represents the mass matrix of the structure, $[C]$ denotes the damping matrix, and $[K]$ is the stiffness matrix. The vector $\{F\}$ signifies the load vector applied to the structure due to fluid forces. The nodal acceleration vector is given by $\{\ddot{u}\}$, the nodal velocity vector by $\{\dot{u}\}$, and the nodal displacement vector by $\{u\}$. For the time discretization of Eq. (4), we employ the Newmark[23] family of numerical time integration schemes. The time domain T is divided into N time steps, each with a duration of $\Delta t = \frac{T}{N}$. Displacements and velocities are computed for each time step using the following equation:

$$\{u_{n+1}\} = \{u_n\} + \Delta t\{\dot{u}_n\} + \Delta t^2\left(\frac{1}{2} - \beta\right) + \Delta t^2\beta\{\ddot{u}_{n+1}\}, \tag{5}$$

$$\{\dot{u}_{n+1}\} = \{\dot{u}_n\} + \Delta t(1-\gamma)\{\ddot{u}_n\} + \Delta t\gamma\{\ddot{u}_{n+1}\}. \tag{6}$$

The parameters $\beta \in [0, \frac{1}{2}]$ and $\gamma \in [0, 1]$ define the characteristics of the numerical method. A modified version (α- method[24]) of the Newmark algorithm can be used for direct integration in dynamic analyses.[25] This α-method extends the Newmark method by incorporating an additional α parameter into the equations of motion, thereby introducing numerical dissipation to enhance stability for $n = 0, 1, 2, \ldots, N-1$,

$$[M]\{\ddot{u}_{n+1}\} + (1+\alpha)[K]\{u_{n+1}\} - \alpha[K]\{u_n\} = \{F_{n+1}\}. \tag{7}$$

C. Strongly coupled partitioned approach

The coupled problem can be solved in either a monolithic or partitioned manner. The monolithic approach solves the fluid and structural equations simultaneously in a single coupled system. In terms of convergence, it requires significantly more memory and computational resources due to the larger, more complex system of equations. Thus, it can be more complicated and computationally intensive, making it less practical for large-scale or highly detailed simulations. Conversely, a partitioned approach allows the use of specialized solvers for fluid and structural components separately, leveraging specialized solvers for each domain. This enhances flexibility and computational efficiency, reducing the overall computational cost compared to the monolithic method and making it suitable for this work. In a partitioned approach, strong coupling can be achieved with the interface method by controlling how many times interface data are being exchanged between the fluid and solid domain within a single solution step. Additionally, the number of degrees of freedom at the interface should be kept at optimum without overconstraining the domains to reduce the computational cost.

Considering u_k as the variables at the k-th time step, and u_{k+1} as the temporary variables at the $(k+1)$-th coupling iteration of the $(n+1)$-th time step, the numerical solution of the fluid and structure at an arbitrary coupling time step $(k+1)$ is given by

$$\widetilde{u}_{k+1} = S \circ F(u_k), \tag{8}$$

$$\widetilde{F}_{k+1} = F \circ S(F_k). \tag{9}$$

The residual on the interface at the $(k+1)$-th iteration is defined as follows:

$$r_{k+1} = \widetilde{u}_{k+1} - u_k = \widetilde{F}_{k+1} - F_k. \tag{10}$$

The convergence of coupling iteration is achieved when $||r_{k+1}||$ is smaller than the predefined convergence criterion ($||r_{k+1}|| < \varepsilon_{abs}$). If convergence is not obtained, for the calculation of the $(k+1)$-th iteration, a reasonable u_{k+1} or F_{k+1} is predicted with interface quasi-Newton with approximation of the inverse of the interface Jacobian matrix by the least-squares relaxation method.[26] The relaxation method uses a relaxation parameter $\omega \in [0, 1]$ to predict the converged solution and stabilize the sub-iterations. For a constant under-relaxation approach, the relaxed value of the kinematic coupling data are computed as a combination of the old, relaxed and the new, unrelaxed value as given by

$$u_{k+1} = (1-\omega)u_k + \omega\widetilde{u}_{k+1}. \tag{11}$$

In this work, the dynamic relaxation factor is employed, calculated using linear extrapolation from the previous sub-iteration solutions, to obtain the converged solution with zero residual.

For a partitioned coupling, the system is centered on the interaction of the fluid and solid domain at their common interface, often called wet surfaces. Certain conditions must be met at the interface to physically couple the two domains. The kinematic consistency of the fluid and solid boundary movements must be maintained at the interface. Additionally, the forces exerted by the fluid and solid on the interface must be in equilibrium. The kinematic and equilibrium conditions are given by the following equations:

$$x_f = u_s \quad \text{and} \quad v_f = \dot{u}_s, \tag{12}$$

$$F_f = -F_s \quad \text{at the interface } \Gamma. \tag{13}$$

At the same time, the energy and the momentum is conserved along the interface, and the interface is used for the interpolation of kinematic quantities between the non-matching grids of fluid and solid domains.

D. Dynamic Mode Decomposition

Dynamic mode decomposition (DMD) is a data-driven method used to extract coherent patterns and dynamic behavior from complex, high-dimensional datasets collected through time-resolved simulations or experiments, offering insights into underlying system dynamics, modes, and frequencies. As shown by Schmid,[27] DMD can simplify large-scale problems by projecting them onto dynamical systems with fewer degrees of freedom. This technique identifies and characterizes transient phenomena, such as oscillations and instabilities, by capturing dominant frequencies and their evolution over time. Having the ability to create reduced-order models from high-dimensional datasets, DMD aids in predicting and controlling system dynamics, providing valuable insights into transient behaviors across various scientific and engineering fields.

Utilizing a time-series matrix D comprised of flow field data matrices u captured at distinct spatial points and time instances, shown as Eq. (14), it is possible to capture the temporal evolution of the entire system through the application of a time transition matrix A,

$$D = [u_0, u_1, \ldots, u_{n+1}]. \tag{14}$$

Two matrices of X and Y, defined by Eqs. (15) and (16), are established from the transient flow fields with the same time interval.

Using matrix A to build a linear relationship between the matrices of X and Y, they are written as

$$X = [u_0, u_1, \ldots, u_n], \tag{15}$$

$$Y = [u_1, u_2, \ldots, u_{n+1}], \tag{16}$$

$$Y = AX. \tag{17}$$

From the result of the singular value decomposition of X, we can obtain the result of the eigenvalue decomposition of A. Due to the increasing computational intricacy associated with eigenvalue decomposition for sizable A matrices, we implement the exact dynamic mode decomposition[19] method. At first, matrix X is decomposed into singular values, selectively employing pertinent modes. Subsequently, matrix A is projected, followed by eigenvalue decomposition. The eigenvector matrix Φ represents the dynamic modes, each contributing uniquely to the system, while the eigenvalue matrix Λ, a complex structure, characterizes system changes (magnitude and amplitude),

$$A\Phi = \Phi\Lambda, \tag{18}$$

$$A = \Phi\Lambda\Phi^{\dagger}, \tag{19}$$

$$Y = \Phi\Lambda\Phi^{\dagger}X, \tag{20}$$

$$u(t) = \Phi\Lambda^{t/\Delta t}\Phi^{\dagger}u(0). \tag{21}$$

Using the eigenvalue matrix Λ, eigenvector matrix Φ, and coefficient matrix vector $\Phi^{\dagger}$, it is possible to reconstruct $u(t)$ from Eq. (21).

III. COMPUTATIONAL SETUP

A. Fluid solver

The SU2[28] code is an open-source unstructured mesh fluid flow solver. The three-dimensional compressible Navier–Stokes equation is the governing equation of this code that consists of the total mass, momentum, and energy conservation laws. The governing equations are translated to the generalized coordinate system and solved using a vertex-centered finite volume technique. The flow has been treated as standard air. The viscous terms are estimated by taking the average of flow property gradients between the cells. The spatial gradient is derived using the Green–Gauss method. Sutherland's formula is used to calculate the viscosity coefficient. Jameson–Schmidt–Turkel scheme[29] is used as an advection method. The implicit dual time-stepping approach with the second-order backward difference is used for time integration. As the matrix solution technique, the Flexible Generalized Minimum Residual (FGMRES) method is used. No turbulence models are considered in the research. For parallel computation of this large problem, the domain decomposition technique and message passing interface are used.

B. Structural solver

CalculiX,[30] an open-source finite element solver, is used to investigate the nonlinear dynamics of the membrane aeroshell utilizing an adapter. Additionally, the nonlinear structural response of the aeroshell subjected to dynamic stress is determined through implicit integration of the equations of motion. The research object is a three-dimensional continuum, with no temperature change during the analysis. The governing equation of structural dynamics is based on the principle of virtual work and discretized with respect to microelements. It encompasses the displacement field within each element, an element stiffness matrix, an element load vector, and an element mass matrix. The load vector, stiffness matrix, and mass matrix are computed for each element. Numerical integration is applied to obtain these matrices and vectors. The α-method is employed with Gauss–Legendre quadrature integration to solve the overall stiffness equation. However, it should be noted that the current approach does not account for the nonlinearity of material characteristics.

C. FSI modeling approach

In the partitioned technique, existing analytic algorithms are used to solve both physics independently while exchanging data at a predefined interval, resulting in a coupled solution. Due to time restrictions, less complexity, and the usage of verified codes, the partitioned coupling strategy is selected for this application. preCICE[31] is a coupling library to couple the flow solver SU2 to the structural solver CalculiX. During the analysis, an adapter, which is a small code for communication between preCICE and solvers, is included for each solver. The coupling process is outlined in Fig. 2. The coupling process assumes that the continuity and equilibrium conditions are consistently fulfilled on the coupled interface. The fluid solver transmits the aerodynamic forces to the coupled interface while receiving displacement information from the structural solver. The coupling library preCICE incorporates nearest-projection data mapping algorithms to facilitate these data exchange between non-matching grids using the parametric elements of the respective grids, enabling efficient information interpolation. Transmission Control Protocol/Internet Protocol sockets have been used to allow for efficient data flow between the solvers. To meet the continuity and equilibrium conditions between physical quantities at the coupled interface with arbitrary accuracy, the parallel-implicit coupling technique is adopted with the interface quasi-Newton[32] convergence acceleration scheme in the iterations. Adopting these schemes increased the computational cost significantly. Nevertheless, the stability of the coupling process increased. After initialization and establishing communication, the fluid and structural domains are iteratively solved inside the solver. At time t, the coupled boundary data are exchanged each time, and the coupled iterations are performed to

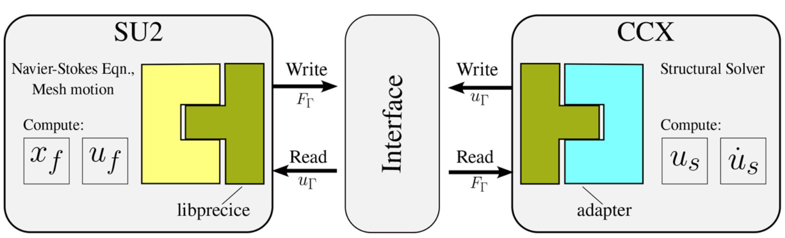

FIG. 2. Strongly coupled partitioned approach using the interface of fluid and solid domain.

satisfy the continuity and equilibrium requirements. After the residuals reach below a set value, the solver moves to the next time $t + \Delta t$.

D. Dynamic mode analysis

For the present study, the spatiotemporal data of structural deformation are extracted at a specific time interval from the coupled simulation to ensure a statistically stable condition. To construct the deformation matrix D [Eq. (14)] for the modal decomposition, instantaneous deformation data are extracted as .vtk files, often called snapshots, spanning the time interval from 0.020 s to 0.095 s. Each of these snapshots are separated by a time interval of 0.0005 s. After the data collection, these data are reshaped in vector forms to perform the modal decomposition. The steps in modal decomposition are illustrated in Fig. 3. The DMD method addressed in Sec. II D is implemented in the open-source modal decomposition code Revun.[33]

Selecting the physically important modes from the DMD analysis is crucial for comprehending the dynamic phenomena and developing reduced-order models to represent that phenomenon. Compressed sensing, introduced to DMD by Jovanovic *et al.*,[34] appears to be a potential way to achieve this. To identify the dynamically significant modes, a greedy approach[35] for compressive mode-sensing is used in this work. In this approach, the most influential DMD modes are identified that help in defining the dynamics of the system. The greedy mode-sensing method is depicted in Algorithm 1. This method iteratively selects the most significant modes that minimize the difference between the real displacement obtained from the FSI result ($\boldsymbol{d}_{\mathrm{FSI}}$) and the reconstructed displacement ($\boldsymbol{d}_{\mathrm{R}}$). The iteration continues until the termination condition is met: $||\boldsymbol{d}_{\mathrm{FSI}} - \boldsymbol{d}_{\mathrm{R}}|| \leq \varepsilon$, where ε is a predefined tolerance. After setting a large initial value for the residual, it iterates through all indices (i) of the size of the DMD modes and calculates the residual $F_i = ||\boldsymbol{d}_{\mathrm{FSI}} - \boldsymbol{d}_i||$. Finally, the index that minimizes the residual is selected. Based on the greedy algorithm, two distinct frequency groups are identified as the primary and secondary modes.

IV. GEOMETRY AND FLOW CONDITIONS

The numerical analyses are carried out on a scaled-down model of the membrane aeroshell, using high-strength ZYLON[36] fabric for both the membrane surface and inflatable torus. The model has a radius of 40 mm for the aeroshell, a membrane thickness of 0.15 mm, and a flare angle of 70°, as shown in Fig. 4. The diameter of the inflatable torus is 6 mm. For simplicity, the study omits the detailed inflation mechanism, focusing solely on the structural and aerodynamic behavior of the aeroshell. The aeroshell is subjected to a uniform flow environment. For this analysis, a Mach number of 0.9 is selected, representing the transonic flow regime, while maintaining a constant

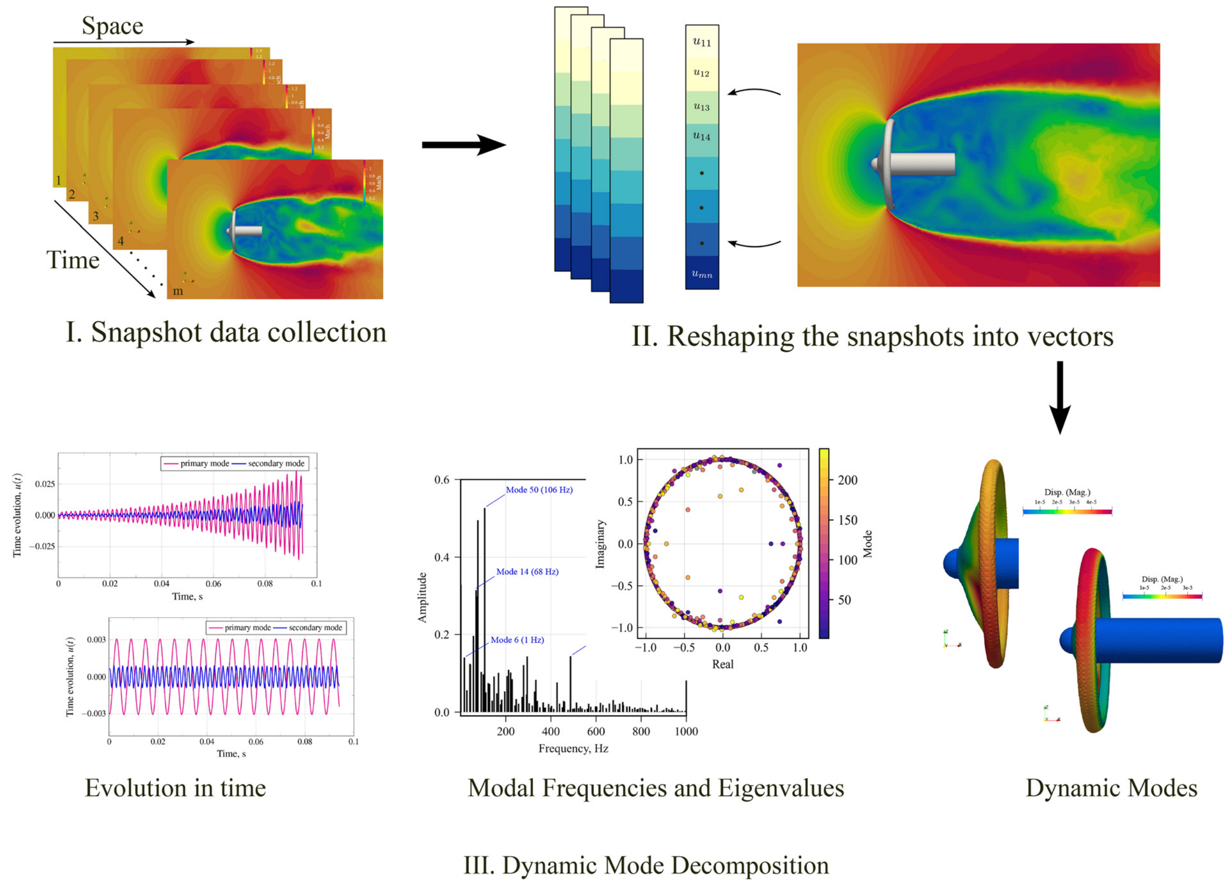

FIG. 3. Steps of modal decomposition of spatiotemporal data for membrane aeroshell.

ALGORITHM 1. Mode-sensing using greedy algorithm.

Input: $\boldsymbol{d}$: displacement reconstructed in mode set $\mathbb{M}$, $\boldsymbol{d}_{\mathrm{FSI}}$: displacement by FSI
Output: $\boldsymbol{d}_{\mathrm{R}}$: displacement accumulated
Initialize solution and index set: $\boldsymbol{d}_{\mathrm{R}} = 0,\ \mathbb{J} = \varnothing$
while not TerminationCondition: $\|\boldsymbol{d}_{\mathrm{FSI}} - \boldsymbol{d}_{\mathrm{R}}\| \leq \varepsilon$ **do**
  Initialize the residual: $F = HugeValue$
  for $i \leftarrow 1 \rightarrow |\mathbb{M}|$ **do**
    if $i \notin \mathbb{J}$ **then**
      Calculate the residual: $F_i = \|\boldsymbol{d}_{\mathrm{FSI}} - \boldsymbol{d}_i\|$
    end if
  end for
  Select index that minimizes the residual: $I = \underset{i \in \mathbb{M}}{\operatorname{argmin}} F_i$
  Add the index: $\mathbb{J} \leftarrow I$
  Update the solution: $\boldsymbol{d}_{\mathrm{R}} \leftarrow \boldsymbol{d}_I$
end while
return Solution

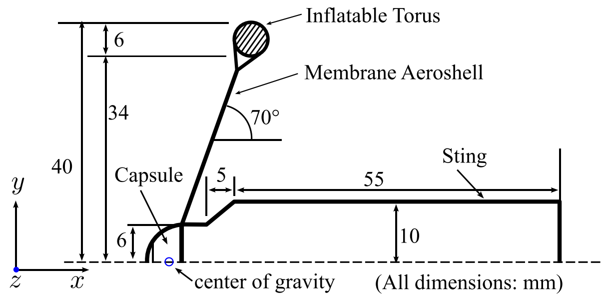

FIG. 4. Geometric dimensions of the research object.

angle of attack of 0° and a freestream dynamic pressure of 7.95 kPa. The freestream Reynolds numbers and other parameters are listed in Tables I and II.

The membrane surface is assumed to be fixed at a temperature of 300 K, with a no-slip condition and no pressure gradient in the normal direction. The computational domain for the fluid flow analysis consisted of 5 231,960 unstructured tetrahedral nodes, as illustrated in Fig. 5. A separate computational mesh having triangular shell elements of 15,532 elements is used for the structural simulation, as shown in Fig. 6. The capsule and the rear sting are treated as fixed boundaries, while the rest are designated as free boundaries and coupled interfaces, allowing for the necessary interactions between the fluid and structural components. As the mechanical properties of ZYLON, Young's modulus was set at 700 MPa, Poisson's ratio of 0.3, and density of 900 kg/m^3.

TABLE I. Calculation conditions for fluid flow.

M_∞	p_∞, kPa	Re_∞	q_∞, kPa	μ_∞, Nsm^{-2}
0.9	150.0	7.049×10^5	7.95	1.529×10^{-5}

TABLE II. Material properties for structural analysis.

Young's modulus, MPa	Density, kg/m^3	Poisson's ratio
700	900	0.30

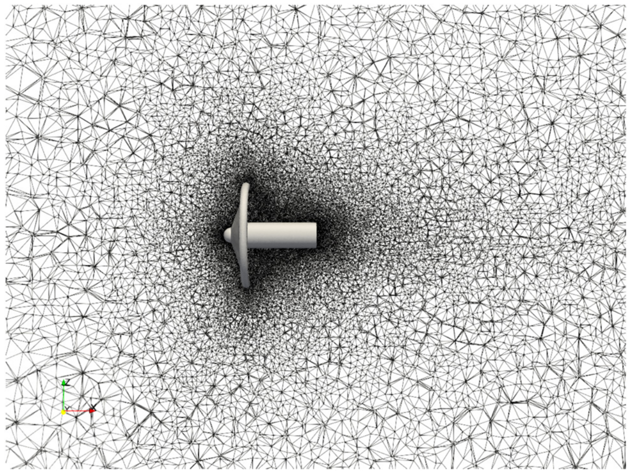

FIG. 5. Computational grids for fluid analysis.

V. RESULTS AND DISCUSSION

A. Eigenfrequency study

Understanding the free oscillation, also known as natural vibrations, is vital to space vehicle design because it reflects the system's inherent dynamic characteristics without the influence of external forces, such as aerodynamic loads. These oscillations depend solely on the system's physical properties, such as mass distribution and

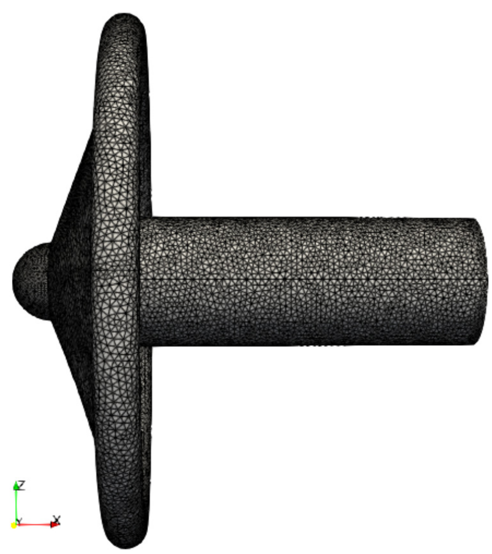

FIG. 6. Computational mesh for structural analysis.

TABLE III. Natural oscillation modes and respective frequencies.

Mode	Frequency
1	59.5
2	59.5
3	211.6
4	353.7
5	393.8
6	394.7
7	763.1
8	763.3
9	772.1
10	772.5

stiffness, and are important for predicting how the structure will behave under various conditions. One critical design objective is to prevent the occurrence of structural resonance, a dangerous phenomenon that arises when the frequency of dynamic loads, such as vibrations from engines or external disturbances, matches the natural frequencies of the structure. This resonance can significantly amplify oscillations, leading to excessive stresses and forces within the material, which, in turn, can cause damage, fatigue, or even catastrophic failure of the space vehicle's components. As space vehicles often operate in extreme environments where structural integrity is paramount, understanding and avoiding resonance is essential for ensuring safety and longevity. So, the natural frequencies and the associated mode shapes of the membrane aeroshell were studied in this work using the finite element solver CalculiX. The eigenfrequency and eigenmodes were obtained by solving the following equation:

$$Kx = \lambda Mx, \tag{22}$$

where K, M, x, and λ are the overall stiffness matrix, overall mass matrix, eigenvector, and eigenvalue, respectively. Table III lists the natural frequencies of the first ten modes. The first to the sixth natural oscillation modes are shown in Fig. 7, and the seventh to the tenth modes are omitted. The first and second modes are pitching and yawing oscillations, respectively, indicating the structural ability to rotate about the vertical and lateral axes. The third mode is the torsional bending in which the membrane surface twists about the x axis. The fourth mode is the first-order translation mode in the x direction, usually called the axial deformation. This mode captures the longitudinal stretching or compressing of the membrane along its length. The fifth eigenmode describes the twisting motion where the structure exhibits rotational displacement. The sixth mode is the first-order bending

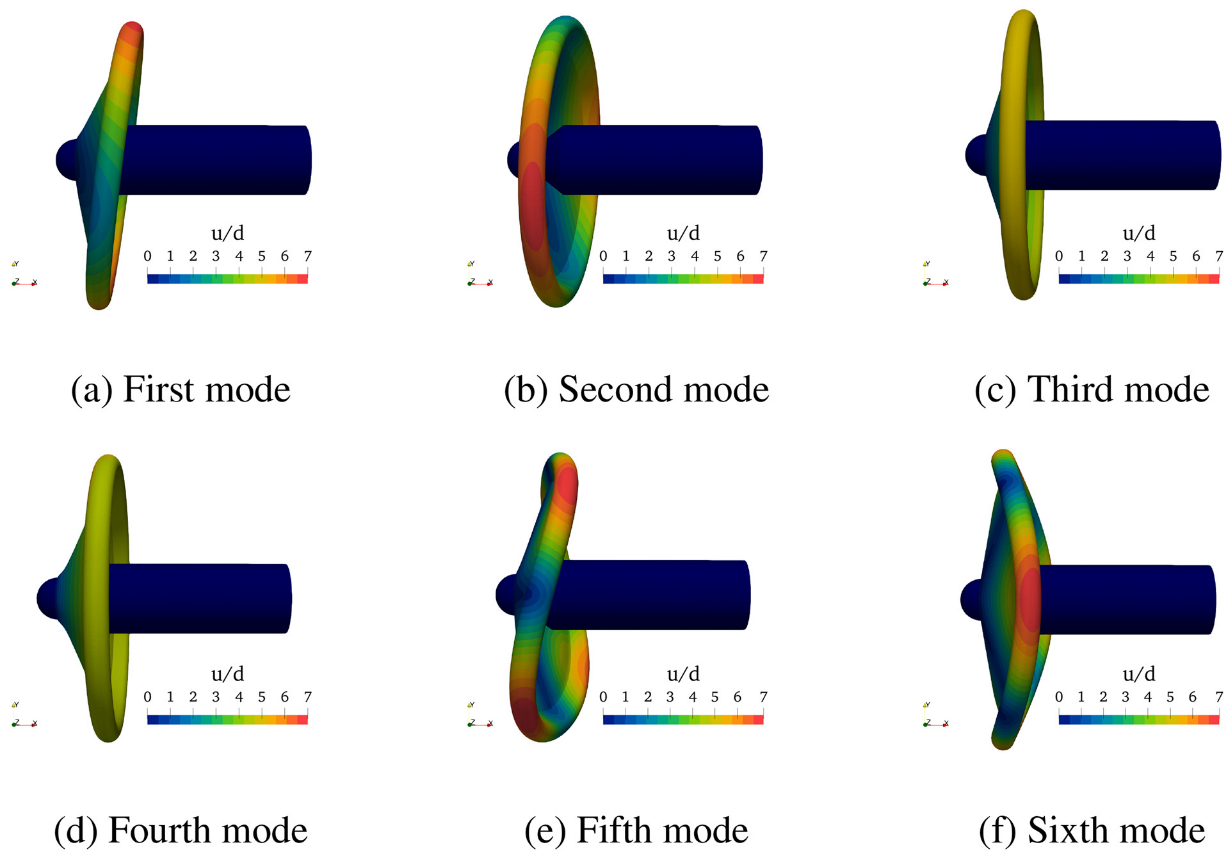

FIG. 7. Natural modes of oscillation.

mode. For the analysis condition of this study, a combination of the first to sixth modes appeared, excluding the third mode.

B. Aerodynamics and elastic deformation

To develop inflatable re-entry vehicle technology, it is essential to evaluate the aerodynamic behavior of membrane aeroshells, given the deformation of their flexible membrane surfaces. As the aeroshell travels through a range of flow conditions during re-entry, assessing its oscillation characteristics is crucial due to its strong relationship with dynamic stability. So, coupled numerical analyses are performed considering the shape deformation. The model is treated as elastic to measure structural deformation under a flow dynamic pressure of 7.95 kPa. The numerical results are then used to decompose and identify the dominant oscillation patterns.

To interpret the results, aerodynamic coefficients are described as follows:

$$C_D = \frac{D}{q_\infty S}, \tag{23}$$

$$C_L = \frac{L}{q_\infty S}, \tag{24}$$

$$C_M = \frac{M}{q_\infty S l}, \tag{25}$$

where q_∞ denotes the dynamic pressure of the freestream, and S is the characteristic area that corresponds to the frontal projected area of the aeroshell. Also, D, L, M, and l are the drag force, lift force, pitching moment, and characteristic length (0.08 m), respectively. The pitching moment was defined around the y-axis, with head-up as positive and the center of moment coinciding with the center of gravity at $(x, y, z) = (0.01, 0.0, 0.0)m$. Additionally, the deformation values are non-dimensionalized by dividing it by the aeroshell diameter $(d = 0.08m)$.

To enhance the stability of the coupled fluid–structure interaction model, the analysis begins with the results obtained from a well-converged steady-state fluid simulation. This approach ensures that the initial conditions for the coupled analysis are as close as possible to the actual flow conditions, thereby reducing the impact of transient loads that could lead to significant deviations in the results caused by the small perturbations in the initial conditions. By minimizing these initial transient effects, the transition to the coupled analysis is smoother, allowing the structure to respond more accurately to the fluid forces without being subjected to abrupt or unrealistic load variations. This method not only improves the numerical stability of the coupled simulation but also enhances the accuracy of the results, as the structure is exposed to realistic flow-induced forces right from the start.

The instantaneous distribution of the Mach number is shown in Fig. 8. No shock wave appears in front of the aeroshell. The large membrane surface area of the inflatable aeroshell leads to flow stagnation, causing a pressure difference between its front and rear regions. An adverse pressure gradient prompts flow separation from the inflatable torus, accompanied by the expansion waves, triggering the formation of alternating vortices and thin shear layers. This dynamic process of wake vortex generation and shedding induces unsteady aerodynamics, manifesting as fluctuations and oscillations in the dynamic behavior of the aeroshell.

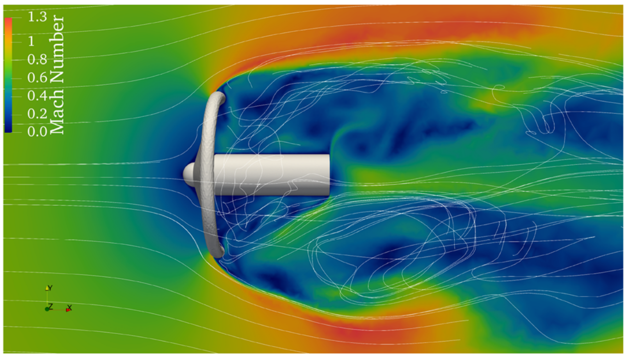

FIG. 8. Instantaneous Mach number distribution.

The wake region behind the aeroshell changes with the unsteady oscillation caused by the separation vortices in the low-speed region directly behind the aeroshell. The symmetric configuration of the aeroshell combined with the presence of the sting prevents a sizeable extent of the development and propagation of small-amplitude high-frequency oscillation.

The instantaneous structural deformation for the analysis condition is shown in Fig. 9. As observed, the membrane exhibits several wrinkles on its surface, indicating complex deformation patterns due to the interaction between the fluid and the structure. These wrinkles are not static; rather, they display transient movement primarily in the circumferential direction, indicating dynamic interaction with the surrounding flow field. This presence of time-dependent aerodynamic forces acting on the membrane causes it to continuously adjust its shape along with an oscillatory swing motion. Such motion results in varying pressure distribution along the membrane surface, as it creates pressure differences that lead to the formation of depressions in areas where the aerodynamic pressure forces are strong enough to push the membrane to deform in the flow direction.

Employing the probe technique, the positional variations of the inflatable torus across distinct positions are tracked. Four probe points

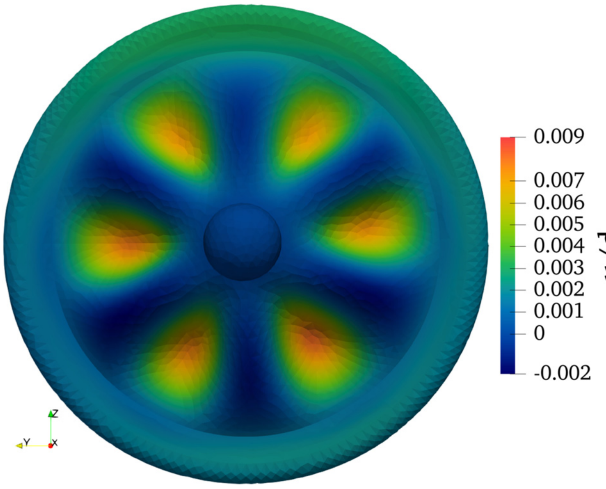

FIG. 9. Instantaneous structural deformation.

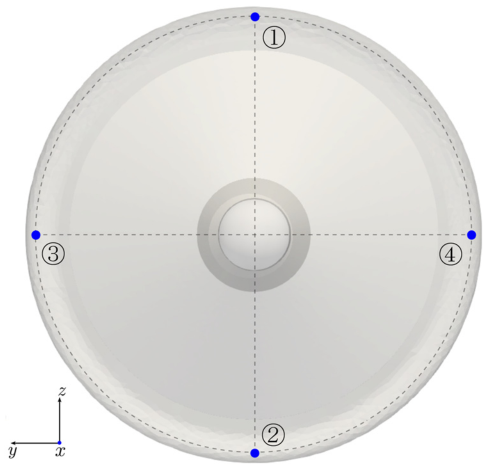

FIG. 10. Locations of the probe points.

are strategically positioned within the structural mesh to evaluate displacement data along the three axes, encompassing the four sides of the aeroshell. The locations of the probe points are shown in Fig. 10.

As shown in Fig. 11, the pitching moment coefficient fluctuates randomly as a result of the oscillation of the aeroshell. Due to the deformation of the membrane surface, the local pressure distribution over the surface changes and aids the transitory oscillation. The absolute value of the pitching moment coefficient is very close to zero which suggests that the body is possibly in a state close to the neutral stability. The drag coefficient value also fluctuates due to pressure variation over the membrane surface, as shown in Fig. 11. The average value of the drag coefficient is around 1.28, close to the value observed in various flight tests.

The instantaneous time-series data reflecting the torus displacement is shown in Fig. 12 in three directions and their frequency plots in Fig. 13. Since the data obtained from the four different probe points shows negligible difference, only probe point (1) data are presented here. The maximum deformation of the membrane surface is around 0.6 mm, which is below 1% of the maximum diameter of the aeroshell. It is self-explanatory from Fig. 12 that the oscillation amplitude is higher in the direction of the flow. However, the periodic oscillation frequencies of the aeroshell appear to be close to each other in every direction.

The fast Fourier transform has been applied to the displacement data in x, y, and z-directions to obtain the frequency of such oscillation. From the frequency domain plot of the torus displacement, as shown in Fig. 13, it is evident that there are two specific peak frequencies present for such oscillations. The first peak frequency is between 169 and 179 Hz for each direction even though the amplitudes are different. The second peak frequencies are higher than 500 Hz. Even though these frequencies are known, it is still insufficient to know if these

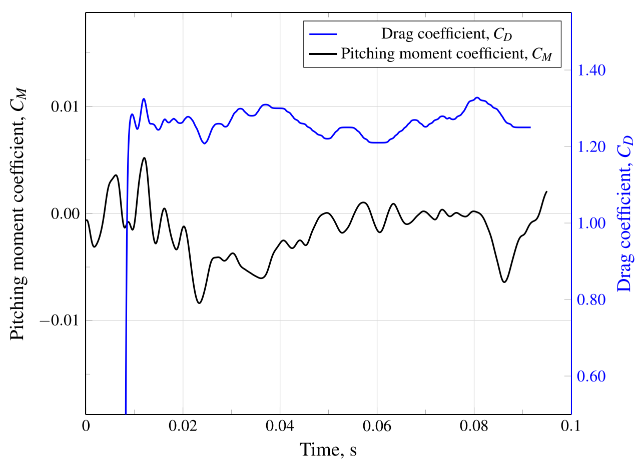

FIG. 11. Time history of instantaneous drag and pitching moment coefficient.

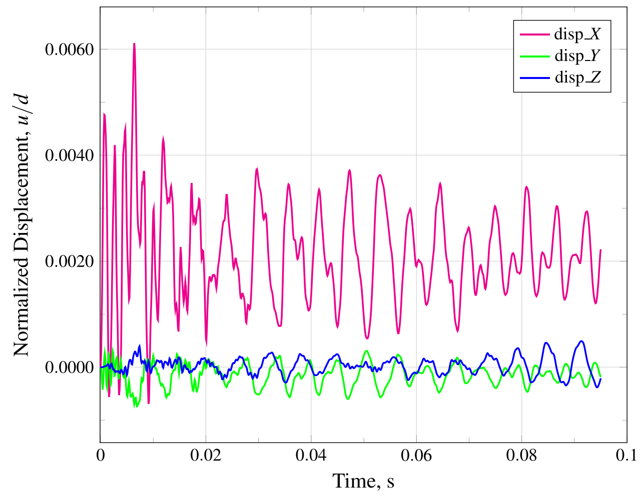

FIG. 12. Time history of instantaneous displacement of torus.

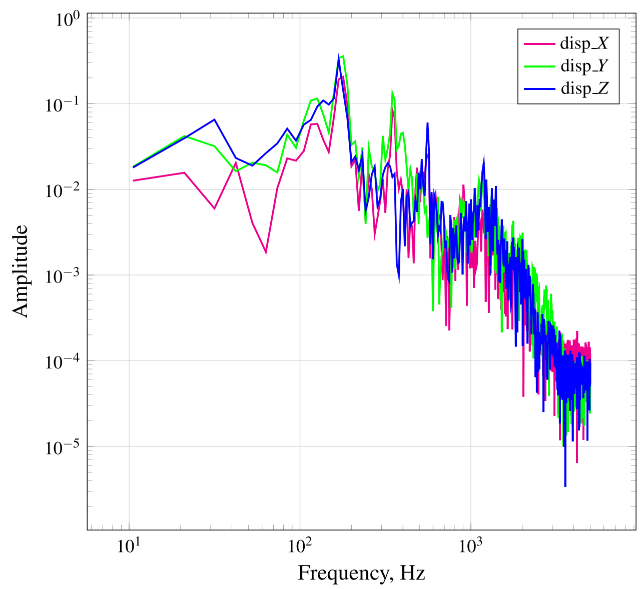

FIG. 13. Frequency plots of torus displacements.

oscillation patterns are dynamically important or not and also how they evolve.

C. Dynamically significant modes

DMD was performed on the structure displacement obtained from the FSI analysis. In this process, DMD was applied to the spatiotemporal data of fluctuations, which were calculated by subtracting the time-averaged value from the instantaneous value. After mode-sensing and reconstruction, the time-averaged value is added to the results. Based on the DMD modes, mode-sensing is performed with the torus displacement history data as a feature to extract the dominant modes. The DMD is executed for a duration ranging from 0.02 s to 0.095 s after the initial state was sufficiently removed in the FSI analysis. Figure 14 shows the amplitude and frequency of each mode obtained from the DMD approach. Most modes are distributed below 1, 000 Hz. The mode with the largest amplitude across the system has a frequency of 26.8 Hz, and modes around 130–190 Hz are also found to be the primary group. However, these modes are not found in the natural oscillation modes. The mode in the frequency of 349.0 Hz is the third peak. However, it is important to note that this trend is based on the spatiotemporal data of the displacement across the entire model. The contribution of each mode when focusing on the displacement at a single point on the torus cannot be determined from this DMD data.

The contribution of each mode was investigated based on the greedy algorithm, using the x-, y-, and z-direction displacements at a point on the torus, i.e., coordinates $(x, y, z) = (0.0145, 0.0, 0.0366)$. Tables IV–VI show the frequencies of the identified significant modes and their coincidence scores, i.e., contributions, based on the L2-norm of the FSI displacement and DMD–reconstructed displacement. In DMD, the extracted modes typically have conjugate modes with reversed frequency signs. Therefore, the conjugate modes are listed in the same row. The modes with frequencies of $\pm$174.5 Hz and $\pm$187.9 Hz have high contributions to the displacements at the probe point on the torus. A high-frequency mode at $\pm$349.0 Hz also played a significant role in the displacements in x- and z-directions. Figures 15(a)–15(c) compare the displacement history reconstructed using the top five modes identified in the DMD results with the FSI analysis results. The complicated deformations in each direction after approximately 0.02 s were appropriately captured with the top five dominant modes.

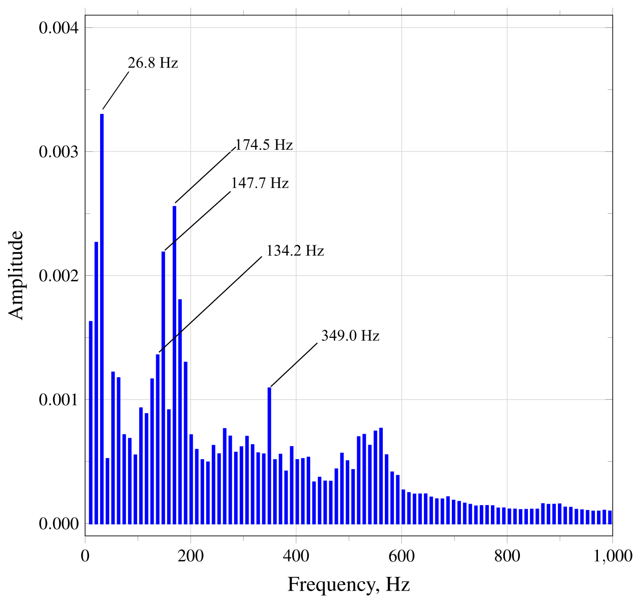

FIG. 14. Amplitude and frequency of DMD modes.

TABLE IV. Frequency and scores of dominant modes for x-displacement.

Rank	Frequency, Hz	Accumulated coincidence
1	$\pm$174.5	0.2156
2	$\pm$187.9	0.3024
3	$\pm$349.0	0.3981
4	$\pm$134.2	0.5086
5	$\pm$161.1	0.5501

TABLE V. Frequency and scores of dominant modes for y-displacement.

Rank	Frequency, Hz	Accumulated coincidence
1	$\pm$174.5	0.3560
2	$\pm$161.1	0.4716
3	$\pm$187.9	0.6148
4	$\pm$134.2	0.6580
5	$\pm$120.8	0.6974

TABLE VI. Frequency and scores of dominant modes for z-displacement.

Rank	Frequency, Hz	Accumulated coincidence
1	$\pm$174.5	0.2167
2	$\pm$349.0	0.2987
3	$\pm$187.9	0.3863
4	$\pm$134.2	0.4759
5	$\pm$161.1	0.5245

Figures 16(a)–16(c) show the DMD-reconstructed modes with frequencies of $\pm$174.5 and $\pm$187.9, and $\pm$349.0 Hz, respectively, which are identified as having high contributions in this mode-sensing analysis. The contours represent the displacement magnitude. The modes at $\pm$174.5 and $\pm$187.9 Hz are similar with each other in displacement behavior, which is composed of the swinging motion with membrane deformation. These combined swinging and membrane deformation modes significantly contribute to the displacement history. However, these two modes do not correspond to any natural oscillation modes. The high-frequency mode at 349.0 Hz was derived by membrane deformation, which also induced the torus displacement. While the frequency of the DMD-reconstructed mode is similar with that of fourth mode of the natural oscillation, the mode is completely different. These results indicate that the reconstructed dominant modes do not necessarily align with the natural oscillation modes. Thus, it

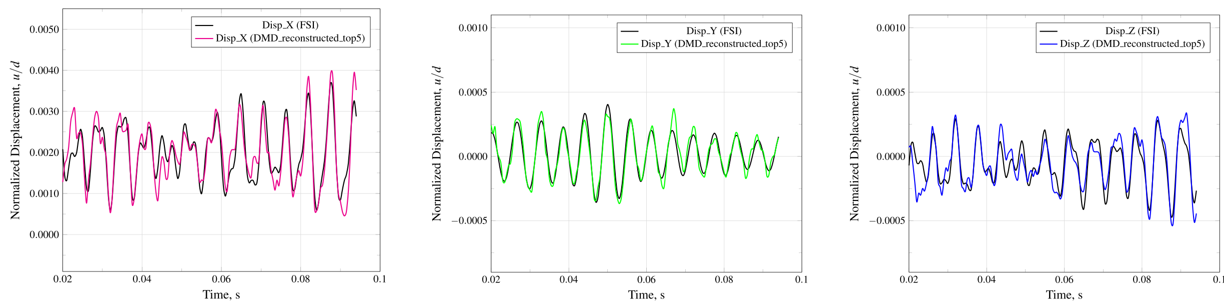

(a) x-direction (b) y-direction (c) z-direction

FIG. 15. Comparisons of displacement between FSI analysis results and reconstructed data considering up to five modes.

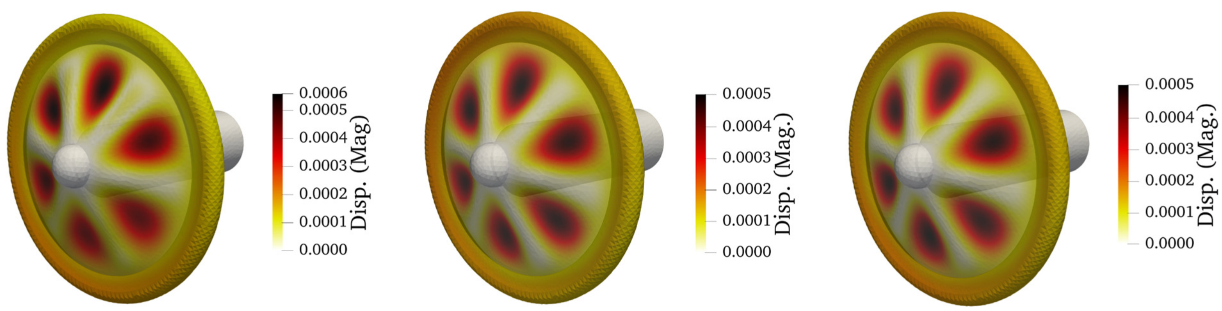

(a) Mode of $\pm$174.5 Hz (b) Mode of $\pm$187.9 Hz (c) Mode of $\pm$349.0 Hz

FIG. 16. Reconstructed modes of each frequency.

suggests that aerodynamic forces strongly influence the deformation of the aeroshell and torus.

VI. CONCLUSION

This research explored the unsteady fluid–structure interaction behavior of a deployable aeroshell in transonic flow, considering the feedback effect of shape deformation. Additionally, dynamic mode decomposition is employed to analyze coherent patterns within the system. Using the greedy compressive sensing algorithm, the dominant membrane deformation structures are identified. The results revealed that the dominant pattern of deformation is the combination of axial deformation and swing oscillation. The frequencies of such dominant modes are around 130–190 Hz. While some modes exhibit higher oscillation amplitudes, they are not significant when considering the overall motion of the aeroshell. These oscillation behaviors observed with modal decomposition show partially similar characteristics and frequencies to those of the eigenfrequency modes; however, they do not coincide completely. This means that the deformation motions of the aeroshell and torus are under the strong influence of aerodynamic forces, where the fluid flow not only excites the natural oscillation modes but also modifies the structural response due to the continuous feedback loop between fluid forces and structural deformation. This study concludes by elucidating the complex interactions between aerodynamic forces and structural responses of the flexible membrane aeroshell through the decomposition of structural deformation. Such insights are essential for improving design strategies and ensuring the reliability of flexible aeroshells in real-world applications.

ACKNOWLEDGMENTS

The authors deeply thank Mr. Hideaki Kominami, FUJIFILM Co., Ltd., for providing valuable advice on the shell element model in the CalculiX software. This study was supported by the JSPS KAKENHI (Grant Nos. 23H00212 and 24K01072). The present computations used computational resources of SQUID provided by the Cybermedia Center, Osaka University, through the Joint Usage/Research Center for Interdisciplinary Large-scale Information Infrastructures (Project ID: EX23706) and the HPCI System Research Project (Project ID: hp240004).

AUTHOR DECLARATIONS

Conflict of Interest

The authors have no conflicts to disclose.

Author Contributions

Sanjoy Kumar Saha: Formal analysis (equal); Investigation (equal); Validation (equal); Visualization (equal); Writing – original draft (equal). **Yusuke Takahashi:** Conceptualization (equal); Funding acquisition (equal); Project administration (equal); Supervision (equal); Writing – review & editing (equal).

DATA AVAILABILITY

The data that support the findings of this study are available from the corresponding author upon reasonable request.

REFERENCES

[1] J. Masciarelli, J. Lin, R. Rohrschneider, R. Bartels, J. Hall, and J. Ware, "Ultra lightweight ballutes for return to earth from moon," in *47th AIAA/ASME/ASCE/AHS/ASC Structures, Structural Dynamics, and Materials Conference 14th AIAA/ASME/AHS Adaptive Structures Conference 7th*, AIAA Paper No. 2006-1698, (2006), p. 1698.

[2] R. R. Rohrschneider and R. D. Braun, "Static aeroelastic analysis of thin-film clamped ballute for titan aerocapture," J. Spacecr. Rockets **45**, 785–801 (2008).

[3] M. J. Miller, B. A. Steinfeldt, and R. D. Braun, "Supersonic inflatable aerodynamic decelerators for use on sounding rocket payloads," in *AIAA Atmospheric Flight Mechanics Conference*, AIAA Paper No. 2014-1092, (2014), p. 1092.

[4] K. Yamada, T. Abe, K. Suzuki, O. Imamura, and D. Akita, "Reentry demonstration plan of flare-type membrane aeroshell for atmospheric entry vehicle using a sounding rocket," in *21st AIAA Aerodynamic Decelerator Systems Technology Conference and Seminar* (2011), p. 2521.

[5] D. Lyons and W. Johnson, "Ballute aerocapture trajectories at Neptune," in *AIAA Atmospheric Flight Mechanics Conference and Exhibit*, AIAA Paper No. 2004-5181, (2004), p. 5181.

[6] K. Yamada, T. Abe, K. Suzuki, N. Honma, M. Koyama, Y. Nagata, D. Abe, Y. Kimura, A. K. Hayashi, and D. Akita, "Deployment and flight test of inflatable membrane aeroshell using large scientific balloon," in *21st AIAA Aerodynamic Decelerator Systems Technology Conference and Seminar*, AIAA Paper No. 2011-2579, (2011), p. 2579.

[7] Y. Takahashi, K. Yamada, and T. Abe, "Examination of radio frequency blackout for an inflatable vehicle during atmospheric reentry," J. Spacecr. Rockets **51**, 430–441 (2014).

[8] K. Yamada, Y. Nagata, T. Abe, K. Suzuki, O. Imamura, and D. Akita, "Reentry demonstration of flare-type membrane aeroshell for atmospheric entry vehicle using a sounding rocket," in *AIAA Aerodynamic Decelerator Systems (ADS) Conference*, AIAA Paper No. 2013-1388, (2013), p. 1388.

[9] K. Yamada, "Structural strength of flare-type membrane aeroshell supported by inflatable torus against aerodynamic force," in *28th ISTS*, Okinawa; ISTS, available at: https://cir.nii.ac.jp/crid/1574231875485229440 (2011).

[10] Y. Nagata, K. Yamada, T. Abe, and K. Suzuki, "Attitude dynamics for flare-type membrane aeroshell capsule in reentry flight experiment," in *AIAA Aerodynamic Decelerator Systems (ADS) Conference*, AIAA Paper No. 2013-1285, (2013), p. 1285.

[11] Y. Takahashi, D. Ha, N. Oshima, K. Yamada, T. Abe, and K. Suzuki, "Aerodecelerator performance of flare-type membrane inflatable vehicle in suborbital reentry," J. Spacecr. Rockets **54**, 993–1004 (2017).

[12] Y. Takahashi, M. Matsunaga, N. Oshima, and K. Yamada, "Drag behavior of inflatable reentry vehicle in transonic regime," J. Spacecraft Rockets **56**, 577–585 (2019).

[13] Y. Takahashi, T. Ohashi, N. Oshima, Y. Nagata, and K. Yamada, "Aerodynamic instability of an inflatable aeroshell in suborbital re-entry," Phys. Fluids **32**, 075114 (2020).

[14] Y. Takahashi, K. Yamada, T. Abe, and K. Suzuki, "Aerodynamic heating around flare-type membrane inflatable vehicle in suborbital reentry demonstration flight," J. Spacecraft Rockets **52**, 1530–1541 (2015).

[15] J. Wu, Z. Zhang, A. Hou, X. Xue, and X. Cao, "Thermal aeroelastic characteristics of inflatable reentry vehicle experiment (IRVE) in hypersonic flow," Int. J. Aerosp. Eng. **2021**, 6673818.

[16] B. Smith, J. Hill, I. Clark, and R. Braun, "Oscillation of supersonic inflatable aerodynamic decelerators at mars," in *21st AIAA Aerodynamic Decelerator Systems Technology Conference and Seminar*, AIAA Paper No. 2011-2516, (2010), p. 2516.

[17] S. Teramoto, K. Hiraki, and K. Fujii, "Numerical analysis of dynamic stability of a reentry capsule at transonic speeds," AIAA J. **39**, 646–653 (2001).

[18] J. J. McNamara and P. P. Friedmann, "Aeroelastic and aerothermoelastic analysis in hypersonic flow: Past, present, and future," AIAA J. **49**, 1089–1122 (2011).

[19] J. H. Tu, "Dynamic mode decomposition: theory and applications," Ph.D. thesis (Princeton University, 2013).

[20] J. Donea, S. Giuliani, and J.-P. Halleux, "An arbitrary Lagrangian-Eulerian finite element method for transient dynamic fluid-structure interactions," Comput. Methods Appl. Mech. Eng. **33**, 689–723 (1982).

[21] F. Palacios, T. D. Economon, A. Aranake, S. R. Copeland, A. K. Lonkar, T. W. Lukaczyk, D. E. Manosalvas, K. R. Naik, S. Padron, B. Tracey *et al.*, "Stanford university unstructured (su2): Analysis and design technology for turbulent flows," in *52nd Aerospace Sciences Meeting*, AIAA Paper No. 2014-0243, (2014), p. 0243.

[22] R. Sanchez, R. Palacios, T. D. Economon, H. L. Kline, J. J. Alonso, and F. Palacios, "Towards a fluid-structure interaction solver for problems with large deformations within the open-source su2 suite," in *57th AIAA/ASCE/AHS/ASC Structures, Structural Dynamics, and Materials Conference*, AIAA Paper No. 2016-0205, (2016), p. 0205.

[23] N. M. Newmark, "A method of computation for structural dynamics," J. Eng. Mech. Div. **85**, 67–94 (1959).

[24] I. Miranda, R. M. Ferencz, and T. J. Hughes, "An improved implicit-explicit time integration method for structural dynamics," Earthquake Eng. Struct. Dyn. **18**, 643–653 (1989).

[25] G. Dhondt, "Calculix Crunchix User's Manual Version 2.12," Munich, Germany, http://www.dhondt.de/ccx 2.19.pdf (accessed September 21, 2017) (2017).

[26] J. Degroote, K.-J. Bathe, and J. Vierendeels, "Performance of a new partitioned procedure versus a monolithic procedure in fluid–structure interaction," Computers Struct. **87**, 793–801 (2009).

[27] P. J. Schmid, "Dynamic mode decomposition of numerical and experimental data," J. Fluid Mech. **656**, 5–28 (2010).

[28] T. D. Economon, F. Palacios, S. R. Copeland, T. W. Lukaczyk, and J. J. Alonso, "Su2: An open-source suite for multiphysics simulation and design," AIAA J. **54**, 828–846 (2016).

[29] A. Jameson, "Origins and further development of the Jameson–Schmidt–Turkel scheme," AIAA J. **55**, 1487–1510 (2017).

[30] G. Dhondt and K. Wittig, *Calculix: A Free Software Three-Dimensional Structural Finite Element Program* (MTU Aero Engines GmbH, Munich, 1998).

[31] H.-J. Bungartz, F. Lindner, B. Gatzhammer, M. Mehl, K. Scheufele, A. Shukaev, and B. Uekermann, "preCICE–a fully parallel library for multi-physics surface coupling," Comput. Fluids **141**, 250–258 (2016).

[32] J. Degroote, P. Bruggeman, R. Haelterman, and J. Vierendeels, "Stability of a coupling technique for partitioned solvers in FSI applications," Comput. Struct. **86**, 2224–2234 (2008).

[33] Y. Takahashi, "Revun: Reconstruction script for VTK/VTU data format based on numerical mode decomposition," Zenodo (2024); available at https://doi.org/10.5281/zenodo.12738925.

[34] M. R. Jovanović, P. J. Schmid, and J. W. Nichols, "Sparsity-promoting dynamic mode decomposition," Phys. Fluids **26**, 024103 (2014).

[35] Y. Ohmichi, "Preconditioned dynamic mode decomposition and mode selection algorithms for large datasets using incremental proper orthogonal decomposition," AIP Adv. **7**, 075318 (2017).

[36] TOYOBO CO LTD, "Zylon (PBO fiber) technical information," https://www.toyobo-global.com/seihin/kc/pbo/zylon-p/bussei-p/technical_201118.pdf (2005) (last accessed June 28, 2024).